Nonperturbative signatures of nonlinear Compton scattering

U. Hernandez Acosta, A. Otto, and B. Kämpfer
Helmholtz-Zentrum Dresden-Rossendorf, 01314 Dresden, Germany
and Institut für Theoretische Physik, TU Dresden, 01062 Dresden, Germany

A. I. Titov
Bogoliubov Laboratory of Theoretical Physics, JINR, Dubna 141980, Russia

(Received 13 May 2020; accepted 16 November 2020; published 23 December 2020)

The probabilities of various elementary laser-photon-electron/positron interactions display in selected phase space and parameter regions typical nonperturbative dependencies such as $\propto \mathcal{P}\exp\{-aE_{\rm crit}/E\}$, where $\mathcal{P}$ is a preexponential factor, $E_{\rm crit}$ denotes the critical Sauter-Schwinger field strength, and E characterizes the (laser) field strength. While the Schwinger process with $a = a_S \equiv \pi$ and the nonlinear Breit-Wheeler process in the tunneling regime with $a = a_{n\ell \rm BW} \equiv 4m/3\omega'$ (with ω' the probe photon energy and m the electron/positron mass) are famous results, we point out here that also the nonlinear Compton scattering exhibits a similar behavior when focusing on high harmonics. Using a suitable cutoff $c > 0$, the factor a becomes $a = a_{n\ell C} \equiv \frac{2}{3} cm/(p_0 + \sqrt{p_0^2 - m^2})$. This opens the avenue toward a new signature of the boiling point of the vacuum even for field strengths E below $E_{\rm crit}$ by employing a high electron beam-energy p_0 to counter balance the large ratio $E_{\rm crit}/E$ by a small factor a to achieve $E/a \to E_{\rm crit}$. In the weak-field regime, the cutoff facilitates a threshold leading to multiphoton signatures showing up in the total cross section at subthreshold energies.

DOI: 10.1103/PhysRevD.102.116016

I. INTRODUCTION

The Schwinger process signals the instability of the vacuum against particle (pair) creation in an external field. The pair (e^+e^-) production rate $\propto \exp\{-aE_{\rm crit}/E\}$, $a = \pi$ [1–3], in a spatiotemporally homogeneous electric field of strength E is exceedingly small due to the large value of the (critical) Sauter-Schwinger field strength $E_{\rm crit} = 1.3 \times 10^{18}$ V/m and therefore escaped a direct experimental verification until now. Much hope was therefore put on the progressing laser technology which however delivers even at present and near-future "ultrahigh intensities" far too low field strengths [4,5]. Many efforts on the theory side attempted to find field configurations which enhance the Schwinger-type pair production. To cite a few entries of the fairly extended literature, which documents the ongoing enormous interest in that topic, we mention dynamical assistance [6–18], double assistance effects [19,20], multibeam configurations [21], and their embedding into optimization procedures [22,23]. In essence, these attempts envisage a reduction of the factor a in the above exponent, which is in general a complicated function of the external parameters. Despite such a "practical goal," these investigations aim at understanding the QED as a pillar of the Standard Model in the nonperturbative, high-intensity regime. Given the seminal meaning of the Schwinger process as paradigm for related processes, e.g., particle production in cosmology [24] and at black hole horizons as Hawking radiation [25], up to the disputed Unruh radiation [26–28], various authors considered analog processes, e.g., in condensed matter physics [29,30] and in wave guides [31], etc., which display also the monomonial, genuinely nonperturbative dependence on an external field parameter.

Still within QED, one can search for more easily accessible processes which have the prototypical nonperturbative dependence $\propto \exp\{-aE_{\rm crit}/E\}$. For instance, the LUXE Collaboration [32–34] envisages to exploit the nonlinear Breit-Wheeler process which is known to behave as $\propto \exp\{-a_{n\ell \rm BW} E_{\rm crit}/E\}$ in the tunneling regime with $a_{n\ell \rm BW} = 4m/3\omega'$, where ω' is the energy of a probe photon traversing a strong laser pulse. LUXE is planed as next-generation follow-up of the seminal SLAC experiment E-144 [35], which operated in the multiphoton regime, by "measuring the boiling point of the vacuum of quantum electrodynamics" [32] via the nonlinear Breit-Wheeler process since $\omega' \gg m$ reduces the exponential suppression, i.e., it makes the above quantity $a_{n\ell \rm BW}$ small when using probe photon energies ω' much larger than the electron

mass m, thus compensating the large value of $E_{\rm crit}/E$ at presently attainable facilities. Note furthermore that the trident process shows also an exponential behavior under certain conditions [36,37], as originally elaborated in [38,39].

Here, we point out that the nonlinear Compton process has a similar nonperturbative exponential field strength dependence under certain side conditions. The key is the suppression of the low harmonics which facilitate the Thomson limit and display a polynomial dependence. What is then left is the otherwise exponentially suppressed contribution. The analogy to the nonlinear Breit-Wheeler process is not surprising since it is the crossing channel of the nonlinear Compton process in the Furry picture. The crucial difference is in the final-state phase spaces. This is most clearly evident in the perturbative, weak-field limit, where the Breit-Wheeler process is a threshold process, while the Compton process without side conditions has no threshold (see [40,41] for the physical regions in the Mandelstam plane). We introduce here as side condition a cutoff which is related to exit channel kinematics. This in fact enforces the exponential behavior.

Our brief note is organized as follows. In Sec. II, we outline the definition of a Lorentz invariant cutoff in the nonlinear Compton scattering. In Sec. III, the restriction of the physically accessible regions in the Mandelstam plane is discussed. The cutoff facilitates a clear signature of multiphoton effects in the total cross section in the weak-field regime (Sec. IV). The moderately strong-field regime is considered in Sec. V, where we compare the exact numerical results with some approximation formula to evidence the exponential dependence of the cross section. The discussion in Sec. VI contains a comparison with laser pulses and outlines of how the cutoff is realized by photon observables in the exit channel. We summarize in Sec. VII.

II. NONLINEAR COMPTON SCATTERING WITH CUTOFF

We consider here a monochromatic laser field in plane-wave approximation for circular polarization. The nonlinear Compton (nℓC) cross section with cutoff c reads

$$\sigma = \frac{\alpha^2\pi}{a_0^2}\frac{1}{k\cdot p}F(a_0, k\cdot p, c),$$
$$F(a_0, k\cdot p, c) = \sum_{n=1}^{\infty}\int_c^{y_n} dx \frac{1}{(1+x)^2}F_n(z_n), \qquad (1)$$

where

$$F_n(z_n) = -4J_n(z_n)^2 + \left(2+\frac{x^2}{1+x}\right) \times a_0^2[J_{n+1}(z_n)^2 + J_{n-1}(z_n)^2 - 2J_n(z_n)^2] \qquad (2)$$

for $c \le y_n$ and $F_n = 0$ elsewhere. The Lorentz and gauge invariant quantity a_0 is the classical nonlinearity parameter characterizing solely the laser beam, and α stands for the fine-structure constant. The arguments of the Bessel functions J_n read explicitly $z_n(x, y_n, a_0) = 2na_0\frac{1}{y_n}\sqrt{\frac{x(y_n-x)}{1+a_0^2}}$, where the two invariants $x = k\cdot k'/k\cdot p'$ and $y_n = 2n\frac{k\cdot p}{m_*^2}$ with $0 \le x \le y_n$ enter. For $c = 0$, one recovers the text book formulas, e.g., in [40,41], where the effective mass $m_*^2 = m^2(1+a_0^2)$ and the (quasi-) momentum balance as well as the relation to asymptotic four-momenta (p/p' for in-/out-electrons and k/k' for in-/out-photons) are discussed in detail. The only but decisive difference is the introduction of the cutoff c in (1) which pushes the lower limit of the x integration to higher values, i.e., it is aimed at suppressing the lower harmonics.

III. KINEMATICS IN THE MANDELSTAM PLANE

The meaning of the cutoff c can be visualized in a covariant manner by inspecting the Mandelstam plane. Defining the invariants $s_n = (q+nk)^2$, $t_n = (k'-nk)^2$, $u_n = (q'-nk)^2$ for harmonics $n = 1, 2, 3\cdots$, the physical regions I–III in scaled triangular coordinates $\hat{s} = s/m_*^2$, $\hat{t} = t/m_*^2$, $\hat{u} = u/m_*^2$ with $\hat{s}+\hat{t}+\hat{u} = 2$ refer to processes related by crossing symmetry on amplitude level: I (red area in Fig. 1) for nℓC process, $e^- + n\gamma \to e^{-\prime} + \gamma'$ or $q + nk = q' + k'$ with quasimomenta q and q', II (upper gray area) for nonlinear Breit-Wheeler (nℓBW) pair production, $\gamma' + n\gamma \to e^+ + e^-$ or $k' + nk = q_{e^+} + q_{e^-}$, and III (left gray area) as mirror of I, e.g., $e^+ + n\gamma \to e^{+\prime} + \gamma'$. In I, the harmonics $\hat{s}_n = $ const are parallel lines (in blue in Fig. 1), limited by $\hat{t} = 0$ (on-axis forward scattering, where $x = 0$) and by the hyperbola $\hat{s}\,\hat{u} = 1$ (on-axis backscattering), i.e., the physical interval of each harmonic is given by $0 \le \hat{t} \le 2 - \hat{s}_n - \hat{s}_n^{-1}$, which is another way of expressing the above quoted restriction $0 \le x \le y_n$. The scaled invariant energy squared of the first harmonic is $\hat{s}_1 = 1 + \Delta\hat{s}$ (measured from the bullet at the top of I in direction of the $\hat{s}$ coordinate, indicated by the arrow, as shown for the other coordinates too) and the spacing of adjacent harmonics is $\Delta\hat{s} = \hat{s}_{n+1} - \hat{s}_n = 2k\cdot p/m_*^2$. Considering an optical laser (we use the frequency $\omega = 1$ eV as representative value) colliding head-on with an electron beam, as available (i) in HZDR[1] (40 MeV [42]) or planned (ii) at ELI[2] (600 MeV [43]) and (iii) at LUXE (17.5 GeV [33]) for instance, one has (i) $\Delta\hat{s} \approx 6.5\times10^{-3}/(1+a_0^2)$, (ii) $9.6\times10^{-2}/(1+a_0^2)$, and (iii) $2.8\times10^{-1}/(1+a_0^2)$ in the red region displayed in Fig. 1. Instead of displaying so many narrow parallel lines representing the harmonics, we depict only a few representative proxies of them at $\hat{s} = \frac{3}{2}, 2, \frac{5}{2}, 3$, etc. as blue lines. In contrast to the perturbative, weak-field limits of the linear processes, $n = 1$, $a_0 \to 0$, the physical regions I–III of the nonlinear processes are mapped out by the discrete harmonics $n = 1\cdots\infty$.

[1]Helmholz-Zentrum Dresden-Rossendorf.
[2]Extreme Light Infrastructure..

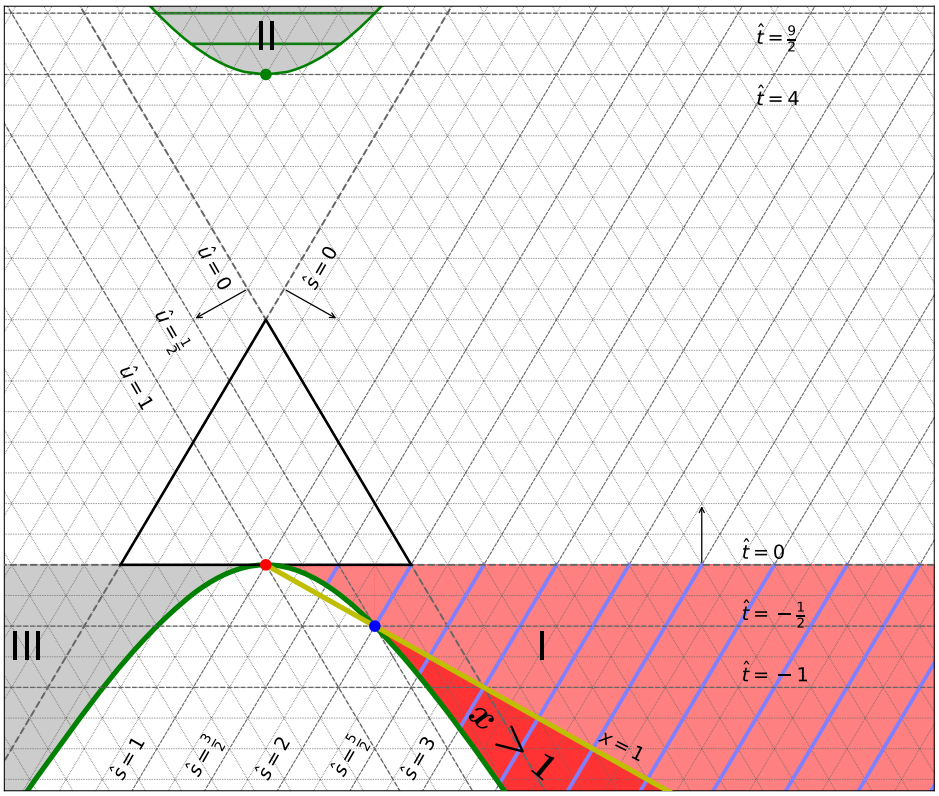

FIG. 1. Mandelstam plane with physical regions of nℓC process (I, red area), nℓBW process (II, upper gray area), and the mirrored Compton I (III, left gray area). Arrows indicate the directions of positive variables $\hat{s}$, $\hat{t}$, and $\hat{u}$, and a few coordinate values are provided too. Bullets depict thresholds. Harmonics of nℓC are parallel to (and may coincide with) the blue lines in region I, which become restricted to the dark-red region (labeled by "$x > 1$") below the boundary $x = 1$ (in yellow) and above the hyperbola $\hat{s}\,\hat{u} = 1$ (green) when imposing the cutoff $c = 1$ which facilitates the threshold at coordinates $\hat{s} = 2$, $\hat{t} = -\frac{1}{2}$, $\hat{u} = \frac{1}{2}$. In region II, the harmonics of nℓBW are parallel to (and may coincide with) the horizontal green lines.

The cutoff $c = 1$ in (1) restricts the region I to the dark-red area, limited by a section of the hyperbola $\hat{s}\,\hat{u} = 1$ and the line $x \equiv k \cdot k'/k \cdot p' = \hat{t}_n/(1 - \hat{s}_n - \hat{t}_n) \geq c$. This excludes the low harmonics $\hat{s}_n < 2$ and restricts the admissible $\hat{t}$ intervals of the harmonics $\hat{s}_n \geq 2$ to $\frac{1}{2}(1 - \hat{s}_n) \geq \hat{t} \geq 2 - \hat{s}_n - \hat{s}_n^{-1}$. For the above quoted numbers, harmonics with $n > (1 + a_0^2)/2p \cdot k$ are in the admissible region. In such a way, a nontrivial threshold is introduced, depicted by the blue bullet at the tip of the dark-red area at coordinates $\hat{s} = 2$, $\hat{t} = -\frac{1}{2}$ and $\hat{u} = \frac{1}{2}$. Imagine now that we keep the laser frequency $\omega = |\vec{k}|$ but lower the electron energy p_0, i.e., the values of $\hat{s}_n$ would become gradually smaller. Then, a certain number of harmonics drop out the admissible area as they pass the threshold by moving to the left above: less and less harmonics contribute to the nℓC process by (i) imposing a threshold by the cutoff $c > 0$ and/or (ii) diminishing $\hat{s}_1$ (and all other $\hat{s}_n$).

IV. MULTIPHOTON REGIME, $a_0 < 1$

To highlight this channel closing effect with invariant variables we exhibit in Fig. 2, the nℓC cross section (1) as a function of $\tilde{s} \equiv 2k \cdot p/m^2$ for $a_0 = 0.01$ and 0.1 for two cutoff values, $c = 1$ and 2. The figure unravels clearly the multiphoton effects which look completely the same as known from nℓBW; see Fig. 3 in [44] (complementary approaches to multiphoton effects are considered in [45]). Thus, the channel closing effect is exactly analog to subthreshold nℓBW pair production in region II [46]. There, the threshold $\hat{t} = 4$ (depicted as bullet at bottom of the green top parabola $\hat{s}\,\hat{u} = 1$ in Fig. 1) limits the physically admissible region: only harmonics with $\hat{t}_n \geq 4$ contribute. The notion "subthreshold" means $\hat{t}_{n=1} < 4$. Similar to the nℓC process, we have displayed in Fig. 1 only two possible proxies (horizontal green lines) of two harmonics of nℓBW in region II. Note that, in considering nℓBW pair production *per se*, one changes usually the coordinate names $\hat{t}_n \to \hat{s}_n$, etc. according to the crossing symmetry relations [41].

V. NONPERTURBATIVE REGIME, $a_0 \gtrsim 1$

After enforcing a nontrivial threshold in nℓC process by the cutoff $c > 0$, one expects a further similarity to the nℓBW in the region $a_0 > 1$ despite different phase

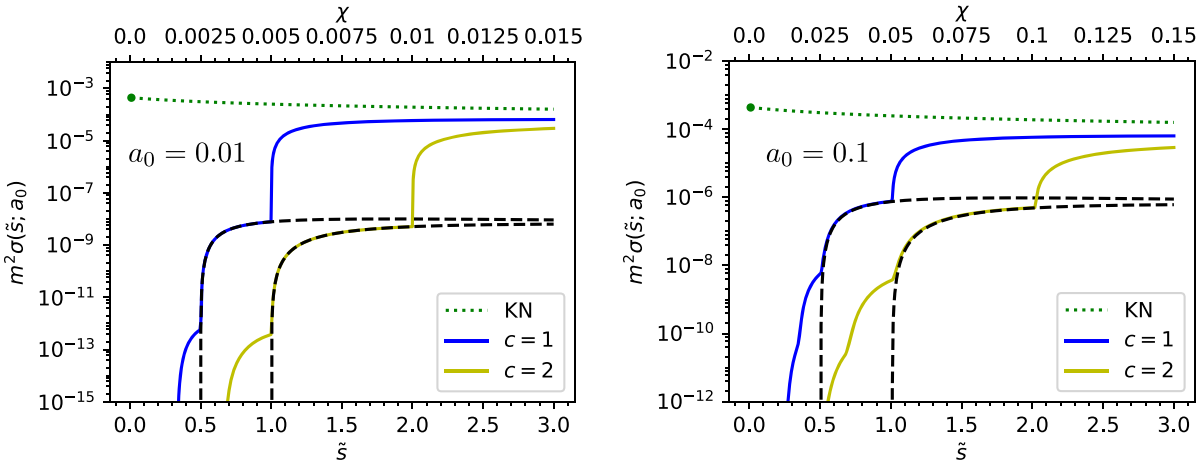

FIG. 2. Scaled cross section of nℓC (1) with cutoff values $c = 1$ (blue curves) and $c = 2$ (yellow curves) for $a_0 = 0.01$ (left panel) and $a_0 = 0.1$ (right panel). The dashed curves depict separately the harmonic $n = 2$. Note the use of the variables $\tilde{s} \equiv 2p \cdot k/m^2 = (s_1 - m_*^2)/m^2$ (bottom abscissa) or $\chi = a_0\tilde{s}/2$ (top abscissa); accordingly, the harmonic thresholds are at $\tilde{s} = c(1 + a_0^2)/n$. For comparison, the Klein-Nishina cross section is depicted by a dotted curve, and the Thomson cross section is marked by a circle. Upon increasing the value of a_0, more and more harmonics are lifted, and at $a_0 = 1$ (not displayed) already a multitude of harmonics adds up to generate smooth distributions in the sub-threshold region, i.e., below $\tilde{s} = 1$ (2) for $c = 1$ (2). These distributions are discussed as functions of $1/\chi$, instead of $\tilde{s}$ or χ, in Sec. V below.

spaces. As shown originally in [47–49], in the tunneling regime $a_0 \lesssim 1/\sqrt{\kappa} \gg 1$, the n$\ell$BW pair creation rate scales as $\propto \kappa \exp\{-8/3\kappa\}$, where $\kappa = a_0 k \cdot k'/m^2$ (here, k and k' are the *in* four-momenta of the laser and probe photons). In head-on collisions, $\kappa = 2\frac{\omega'}{m}\frac{E}{E_{\rm crit}}$ since $a_0 = \frac{m}{\omega}\frac{E}{E_{\rm crit}}$. That yields the Schwinger-type dependence $\propto \exp\{-a_{n\ell{\rm BW}}E_{\rm crit}/E\}$ with $a_{n\ell{\rm BW}} = \frac{4}{3}\frac{m}{\omega'}$. The large ratio $E_{\rm crit}/E$ can be compensated by a small ratio m/ω', thus making the pair creation rate accessible in present day experiments by using hard probe photons with $\omega' \gg m$, in contrast to the plain Schwinger rate, even with assistance effects. As emphasized in [32], such a Schwinger-type rate of nℓBW is found numerically already for $a_0 \gtrsim 1$ and $\kappa \lesssim 1$.

Quite in contrast to nℓBW, the nℓC cross section without cutoff displays a polynomial dependence on the invariant Ritus variable[3] $\chi \equiv a_0 k \cdot p/m^2 = a_0(s_1 - m_*^2)/2m^2$ [48]. However, imposing the cutoff $c > 0$, thus suppressing the low harmonics in (1) by a threshold, turns the behavior to an exponential one. In fact, evaluating (1) numerically, one obtains the solid curves in Fig. 3 for $c = 1$ (left panel) and 2 (right panel). Since at $1/\chi < 1$ the curves display an a_0 dependence, we have employed scaling factors. Without the latter ones, the curves at $1/\chi > 1$ are nearly perfectly on top of each other, i.e., independent of a_0. To quantify the $1/\chi$ dependence, we depict for a comparison the dashed/dotted curves based on

$$F_\infty(\chi, c) = \sqrt{\frac{2}{3}}\frac{\chi}{\pi} f(c) \mathrm{erfc}\left(\sqrt{\frac{2c}{3\chi}}\right) + \mathcal{O}(\chi^{2/3}) \overset{c\gg\chi}{\to} \left(\frac{\chi}{\pi}\right)^{3/2} \frac{f(c)}{c} \exp\left\{-\frac{2c}{3\chi}\right\} + \cdots, \tag{3}$$

where $f(c) = (5 + 7c + 5c^2)/(1 + c)^3$ and "erfc" stands for the complementary error function.

One avenue to (3) is to start with (1) in the limit $a_0 \to \infty$ with side condition $(1 - z_n^2/n^2)a_0^2 = \text{const}$ and then to convert the sum via the Euler-Maclaurin formula into an integral, $F_\infty(\chi, c) = -\frac{4}{3\pi}\chi^{2/3}\int_c^\infty dx f(x) x^{-2/3} Ai'(z(x))$ with $z(x) = (x/\chi)^{2/3}$. Under the condition $c \gg \chi$, the derivative of the Airy function, Ai', can be replaced by its asymptotic representation and the integral can be executed upon a shift of the variable x and a suitable Taylor expansion.

Surprisingly, the small-χ leading-order term $\propto \exp\{-2c/3\chi\}$ in (3) numerically approximates (1) fairly well in the nonasymptotic region, $a_0 \gtrsim 1$ and $\chi < 1$, irrespectively, of the assumptions made in the sketched derivation. As a consequence, the nℓC cross section also displays a Schwinger-type dependence $\sigma(c > 0) \propto \exp\{-a_{n\ell C}E_{\rm crit}/E\}$ for suitable values of the cutoff $c > 0$, in general with $a_{n\ell C}(c, a_0, s_1)$. That is, the paradigmatic transmonomial behavior [52] is provided not only for pair creation but shows up also in high-harmonics Compton scattering on the level of "total" cross section, which

[3]The Ritus variable χ is a measure of the field strength $E/E_{\rm crit}$ in the rest frame of the electron; χ encodes the energy of the laser + electron beams as well as the laser intensity. The high-energy limit and the high-intensity limit do not commute albeit they yield both a high-χ asymptotic [50,51].

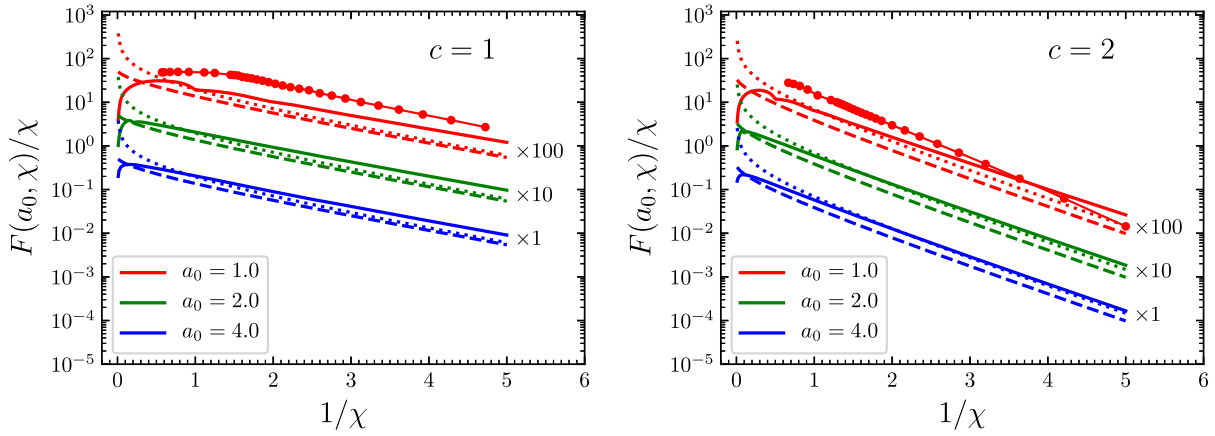

FIG. 3. Normalized cross section $m^2\sigma(\chi)a_0/(\alpha^2\pi) = F(\chi)/\chi$ of nℓC from (1) as a function of $1/\chi$ (solid curves) with cutoff values $c = 1$ (left panel) and $c = 2$ (right panel). The dashed (dotted) curves exhibit the approximation (3) with erfc (exp). For $a_0 = 1$, 2, and 4 from top to bottom with scaling factors as indicated. The red bullets mark results of QED calculations with bandwidth and ponderomotive effects for $a_0 = 1$ (see subsection VI C). Fits of these data by $m^2\sigma(\chi) \propto \exp\{-2c^c_{\rm fit}/3\chi\}$ within the interval $1/\chi = (1, 5]$ deliver $c^{c=1}_{\rm fit} = 1.27$ and $c^{c=2}_{\rm fit} = 2.59$.

actually means integration over a fraction of the out-phase space.

VI. DISCUSSION

A. Imposing the cutoff: kinematics

The cutoff $c > 0$ in (1) looks quite innocent, but in practice it may become challenging. To illustrate that feature, let us employ laboratory observables: $\nu \equiv \omega/m$ ($= 2 \times 10^{-6}$ for optical lasers), $p_0/m = \cosh\zeta$ the Lorentz factor of the in-electron, $\nu' \equiv \omega'/m$ for the normalized energy of the out-photon in direction Θ' such that $\Theta' = 0$ and $\Theta' = \pi$ mean on-axis forward scattering and on-axis backscattering, respectively. Adopting the notation in [40], we recall the relation

$$x = \frac{(1 - \cos\Theta')\nu'}{e^{\zeta} - (1 - \cos\Theta')\nu'}. \tag{4}$$

The admissible intervals for a harmonic n are for head-on collisions $0 \le x \le y_n \equiv 2n\nu e^{\zeta}/(1 + a_0^2)$, $n\nu \le \nu'_n \le n\nu/(1 + 2\kappa_n e^{-\zeta})$ for $2\kappa_n \equiv 2n\nu - e^{\zeta} + (1 + a_0^2)e^{-\zeta} < 0$ or $n\nu/(1+2\kappa_n e^{-\zeta}) \le \nu'_n \le n\nu$ for $\kappa_n > 0$, and $0 \le \Theta' \le \pi$. One has also to recall the well-known nℓC kinematic relation $\nu'(n, \Theta'; a_0, \nu, \zeta) = n\nu/[1 + \kappa_n e^{-\zeta}(1 - \cos\Theta')]$, e.g., in relating the x and Θ' coordinates: a point at $x = \xi y_n$ corresponds to $(\pi - \Theta')^2 \approx 4\frac{1-\xi}{\xi}(1 + a_0^2)e^{-2\zeta}$, independent of the harmonic number. This highlights the preference of backscattering in the relativistic regime, since a significant fraction of events with $x \to y_n$ is seen at $\Theta' \to \pi$.

These relations evidence that one has to reject events with too low values of ν' or select sufficiently high harmonics to realize the request $x \ge c$, see the left panel of Fig. 4 for on-axis backscattering. The meaning of these curves is that the realization of $x \ge c$ requires in general $\nu'(n, \Theta'; a_0, \nu, \zeta) \ge \nu'(x, \Theta'; \zeta)$ either as a function of n (left panel, for $\Theta' = \pi$) or as a function of Θ' (right panel, for selected harmonics), where (4) determines the ν-independent function $\nu'(x, \Theta'; \zeta)$. These relations are exhibited also in the right panel of Fig. 4, where the light-blue region depicts the range wherein $x \ge c = 1$ is fulfilled. In the preferred backward direction $\Theta' \to \pi$, the curves $\nu'(x, \Theta'; \zeta)$ (black dashed) are nearly horizontal, with the benefit that only an energy-resolved measurement is necessary to select the wanted range $x \ge c$ by imposing a veto for all events with $e^{2\zeta}(1 - \cos(\pi - \Theta')) > 20$, for instance. At smaller angles Θ', i.e., going further to the right—beyond the region displayed in the right panel of Fig. 4—the curves $\nu'(x, \Theta'; \zeta)$ bend up, which would require also an angular-resolved measurement. However, the contributions of the very high harmonics are exceedingly small in that phase space region and can be neglected. Altogether, a cross section measurement in backward direction and above the threshold value $e^{\zeta}\nu' \ge 0.25$ facilitates the cutoff $c = 1$ for the LUXE kinematics.

B. Dead cone

In addition to this purely kinematic relations, one has to account for the dynamics, in particular the dead cone effect which is special for circularly polarized lasers according to (1): ignoring for the moment being the cutoff, the harmonics $n > 1$ are (multiply) peaked within the interval $0 < x < y_n$ and drop smoothly toward zero at the boundaries $x \to 0$ and $x \to y_n$. Transforming to the laboratory frame, the angular differential cross sections $d\sigma_n/d\cos\Theta'$ of selected harmonics $n > 1$ are peaked as exhibited in Fig. 5 (left). Only the $n = 1$ harmonic remains nonzero for

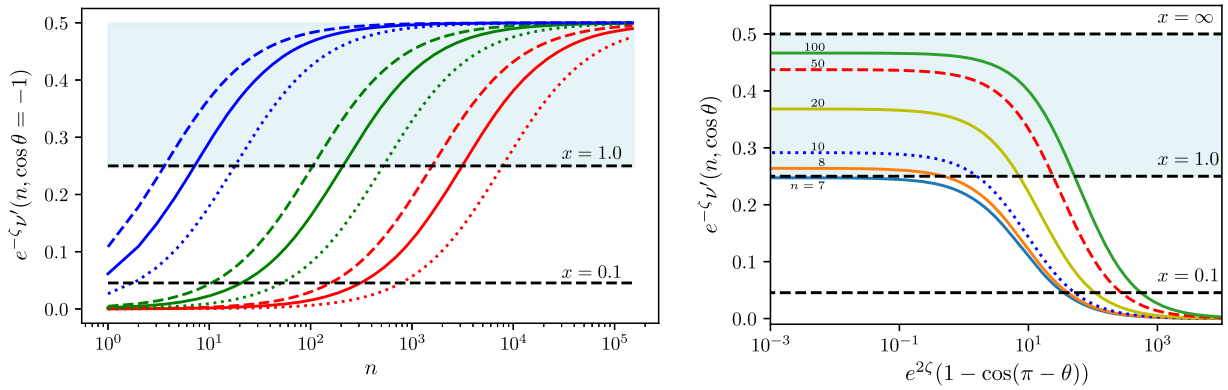

FIG. 4. Left panel: the scaled out-photon energy ν' as a function of the harmonic number n for three kinematic situations referring to the entrance channels at LUXE (left, in blue), ELI (middle, in green), and HZDR (right, in red). For $a_0 = 0.01$ (dashed), 1 (solid), and 2 (dotted) and on-axis backscattering. The curves connect smoothly the values of ν' at the discrete harmonic numbers n. Selecting the out-channel with $x \geq c$ means accepting only events in the light-blue region if $c = 1$ is chosen. Right panel: the scaled out-photon energy as a function of the angle Θ' for the harmonics $n = 7$, (black thin), 10 (blue dotted), 20 (red solid), 50 (green dashed), and 100 (black thin) (LUXE parameters). Note the relation $1 - \cos(\pi - \Theta') \approx \frac{1}{2}\vartheta'^2$ for backscattering, where $\vartheta' = \pi - \Theta'$ measures the angle of the out-photon relative to the in-electron direction. The seemingly horizontal dashed lines $e^{-\zeta}\nu' = \frac{x}{1+x}\frac{1}{1-\cos\Theta'}$ are depicted for three values of the invariant quantity $x = 0.1$, 1, and ∞, and the light-blue region is again for admissible events if $c = 1$ is chosen. The harmonic $n = 7$ does never enter the light-blue region.

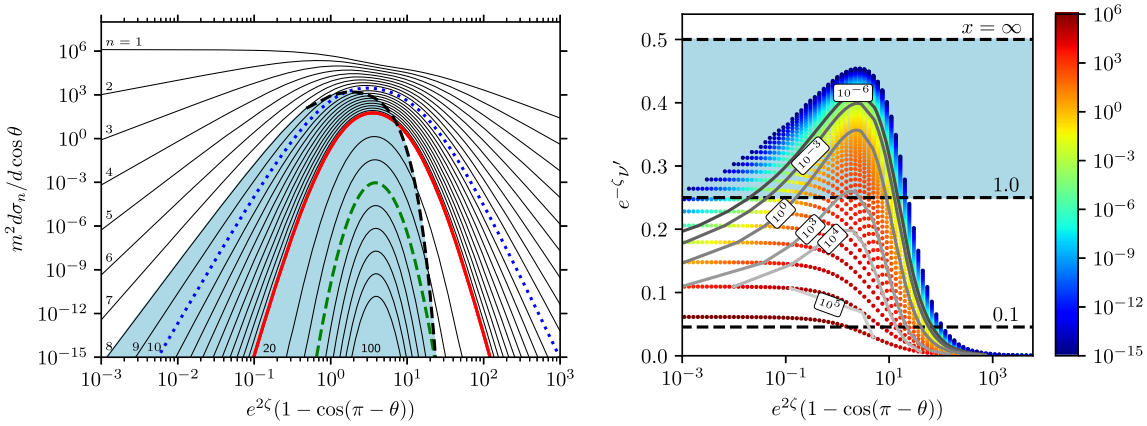

FIG. 5. Left panel: angular differential cross sections $m^2 d\sigma_n/d\cos\Theta' = \frac{\alpha^2\pi}{a_0^2}\frac{m^2}{k\cdot p}\frac{e^\zeta}{n\nu(1-\cos\Theta')^2}\frac{x^2}{(1+x)^2}F_n(z_n)$ with x and z_n to be viewed as functions of Θ' (cf. [40]) for the harmonics $n = 1\ldots20$ (in steps of 1) and $20\cdots100$ (in steps of 10). The harmonics $n = 10$ (blue dotted), 20 (read solid), and 50 (green dashed) are depicted in color code and line style as in Fig. 4 (right); the other harmonics (black solid) are partially labeled. The black dashed curve—to be continued by the harmonic $n = 8$—limits the admissible range (in light blue) where $x \geq c = 1$ is fulfilled. Right panel: angular differential cross sections $m^2 d\sigma_n/d\cos\Theta'$ (see color code on rhs) over the scaled ν'-Θ' plane. Low-order harmonics are clearly separated for monochromatic lasers (but are smeared out for pulses; see below). The gray lines connect points of equal values (given by the numbers in the boxes) of $m^2 d\sigma_n/d\cos\Theta'$ on adjacent harmonics. Contributions smaller than 10^{-15} are not displayed. Both panels are for the LUXE kinematics with $\nu = 2\times10^{-6}$, $e^\zeta = 7\times10^4$, and $a_0 = 1$.

$\Theta' \to \pi$. The dropping of $d\sigma_n/d\cos\Theta'|_{n>1}$ at the left side is the dead cone effect. The dropping at the right side refers to the suppression of forward scattering, i.e., at $\Theta' \to 0$. The black dashed curve connects the points of intersections of the curves $\nu'(n,\Theta';a_0,\nu,\zeta)$ and $\nu'(x=1,\Theta';\zeta)$, which can be read off in Fig. 4 (right) for $n = 10$, 20, 50, and 100. For $n < 8$, there are no such intersections and, as a consequence, the harmonic $n = 8$—left beyond the dashed curve—limits the admissible region $x \geq c = 1$ which is highlighted in light blue, as in Fig. 4.

As advertised above, the contributions of the high harmonics at $e^{2\zeta}(1-\cos(\pi-\Theta')) > 20$ are exceedingly small, thus substantiating our claim that imposing a frequency threshold is enough for a measurement of $\sigma(c=1)$, at least for the here employed LUXE kinematics. This is evidenced in Fig. 5 (right), where some proxy of a

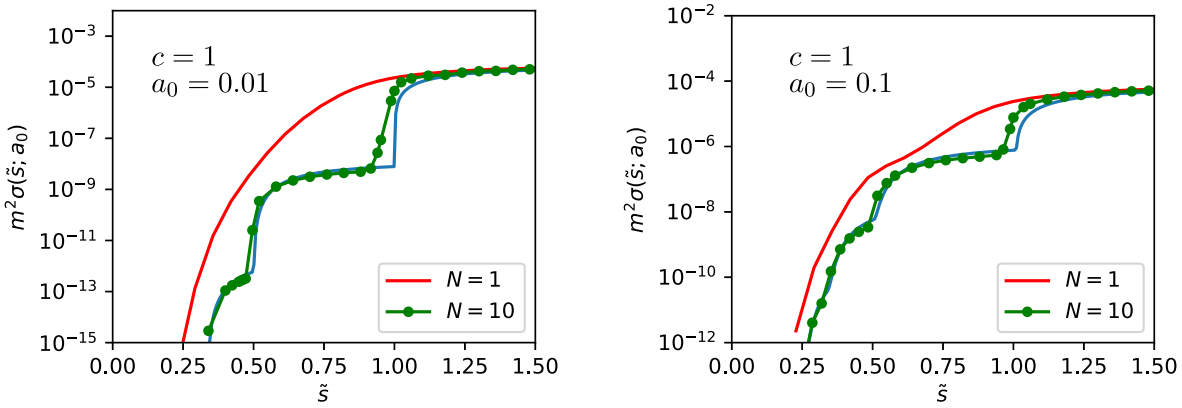

FIG. 6. Same as in Fig. 2 but for laser pulses with envelope shape $g(\phi) = 1/\cosh(\phi/N\pi)$. $N = 1$ (red curves) represents ultrashort pulses and $N = 10$ (green curves marked by dots) is among currently available short pulses. Blue curves are as in Fig. 2 for the monochromatic case. For the cutoff value, $c = 1$ and $a_0 = 0.01$ (left panel) and 0.1 (right panel).

contour plot (gray lines) of the angular differential cross sections $m^2 d\sigma_n/d\cos\Theta'$ is exhibited over the scaled ν'-Θ' plane. [The harmonics n have only support on the curves $\nu'(n, \Theta'; a_0, \nu, \zeta)$ (see Fig. 4, right for several values of n), and the colored pixels encode the values of $m^2 d\sigma_n/d\cos\Theta'$. The gray lines connect points of equal strengths on adjacent harmonics, thus serving as contour lines despite the discrete occupancy in ν' direction.] The experimental challenge is therefore the precise setting of a frequency threshold to select $x \geq c$ events out of a large background.

C. Bandwidth effects and ponderomotive broadening

While (1) is for monochromatic laser beams with the four-potential $\vec{A}(\phi) = g(\phi)[\vec{a}_1 \cos\phi + \vec{a}_2 \sin\phi]$ of the e.m. field with invariant phase ϕ and obeying $g(\phi) = 1$, $\vec{a}_1\vec{a}_2 = 0$, $\vec{a}_1{}^2 = \vec{a}_2{}^2$, one has to check whether laser pulses[4] are well approximated when focusing on total cross sections. In Fig. 6, the cross section as a function of $\tilde{s}$ is exhibited, for $a_0 = 0.01$ and 0.1 as in Fig. 2, however, for short and ultrashort pulses. The QED calculations are based on Eqs. (40) and (42) in [45] (version v1) with $u \geq c$ to impose the cutoff. The pulse shape envelope is here especially $g(\phi) = 1/\cosh(\phi/N\pi)$, where N characterizes the number of oscillations of the field. This envelope $g(\phi)$ does have neither an extended flat-top section nor narrow ramping sections. The former property makes it quite different to a near-monochromatic beam with broad flat-top envelope and may be considered as representing a "worst case"in that respect. The related bandwidth effects and longitudinal ponderomotive broadening are fully included in the QED calculation of one-photon emission in [45]. For short pulses, these effects smoothen the steplike shape of the total cross sections, as known from nℓBW [44]. In particular, for the ultrashort pulse with $N = 1$ (red curves), the combined strong bandwidth effect and ponderomotive broadening overwrite completely the multiphoton effects; the cross section is stark enhanced in the subthreshold region. However, for sufficiently long pulses with $N \geq 10$, i.e., a pulse duration of > 30 fs for optical laser pulses, even without pronounced temporal flat-top profile, the essential dependencies of the cross section model with cutoff (1) are recovered; see green curves marked by dots in Fig. 6 for $a_0 = 0.01$ and 0.1 and red curves marked by bullets in Fig. 3 for $a_0 = 1$. Since the normalization of cross sections in pulses is special (cf. [45,56]), let us focus on slopes at $a_0 = 1$. As noted in the caption of Fig. 3, the slope parameters $c^c_{\rm fit}$ of the pulse model with $N = 10$ are about 25% larger than the ones of the monochromatic model (1). Despite these differences, the ratio is still 1:2. Such a cutoff dependence can be experimentally tested in the analysis of a given data set after data taking, e.g., at a suitable value of χ. (A comprehensive theoretical study of the $a_0 > 1$ dependence must be postponed because our present numerical implementation restricts us to $a_0 \leq 1$.)

Turning to details of differential observables, the model (1) is in general a less useful guide. In fact, keeping the above pulse shape parametrization by $g(\phi) = 1/\cosh(\phi/N\pi)$, the differential cross section $d\sigma/d\omega'|_{\Theta'}$, e.g., for $e^{2\zeta}(1 - \cos(\pi - \Theta')) = 3$ (i.e., for Θ' at about the maximum of the angular differential cross section in Fig. 5, left) does hardly recover the harmonic structures which can be deduced from the right panels of Figs. 4 and 5; even for longer pulses, see the left panel in Fig. 7. Instead of clearly recognizable peaks at $\omega' = m\nu'(n, \Theta'; a_0, \nu, \zeta)$, the spectrum in Fig. 7 (left) displays some complexity which is further obscured by increasing gradually the parameter N.

[4]The Fourier-zero mode of the nonlinear phase can not be longer absorbed in a redefinition of the electron momentum as quasimomentum [53], which is a key quantity in the monochromatic laser beam model (1), but an expansion into harmonics is still possible for smooth, long pulses [53,54] (cf. [55] for a discussion of these issues and a compendium of one- and two-photon emission off electrons in laser pulses).

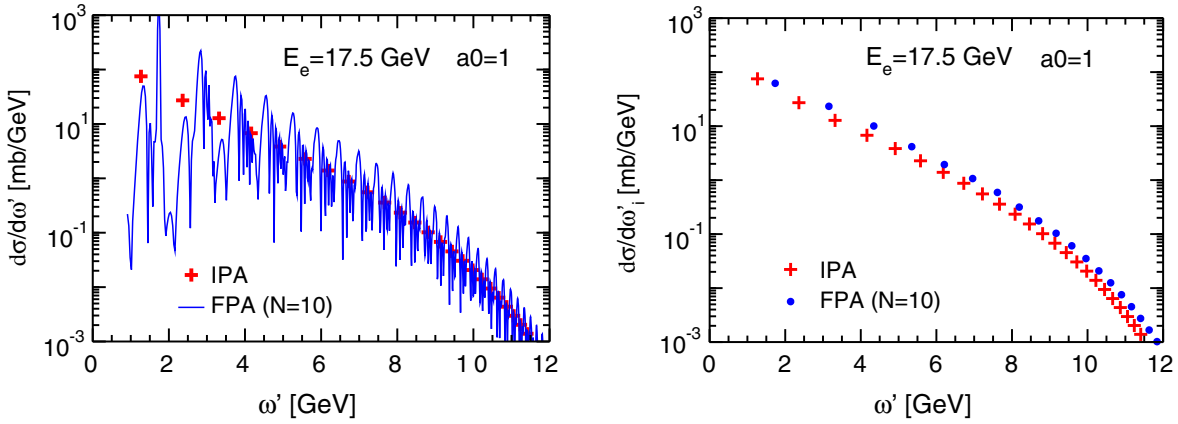

FIG. 7. Left panel: the differential spectrum $d\sigma/d\omega'|_{\Theta'}$ as a function of ω' at polar angle Θ' determined by $e^{2\zeta}(1-\cos(\pi-\Theta'))=3$ for the $1/\cosh(\phi/N\pi)$ pulse envelope with $N=10$ (blue curve). The corresponding QED calculation is as in Fig. 5 of [56] but for the LUXE kinematic parameters used in Fig. 5. Red pluses mark the peak positions in the monochromatic model (1). Right panel: the same as in the left panel but with locally averaged cross section (blue bullets) over the intervals $\omega'(\ell-0.5)\cdots\omega'(\ell+0.5)$ for the internal auxiliary variable $\ell=1,2,3\cdots$ (cf. q. (16) in [56]). The legends adopt the nomenclature in [56]: IPA stands for the monochromatic laser beam and FPA denotes the laser pulse model.

This feature is known since some time, cf. [53,56,57] for instance. Bandwidth effects and ponderomotive broadening have been identified as responsible, together with interferences.

To highlight the impact of the former ones, it is instructive to cast the above nℓC kinematic relation $\nu'(n,\Theta';a_0,\nu,\zeta)$ in the form

$$2e^{-\zeta}\nu'=\frac{1}{1+\frac{e^{-\zeta}}{2n\nu\mu}(1+a_0^2(\phi))+e^{2\zeta}(1-\cos(\pi-\Theta'))\frac{e^{-\zeta}}{4n\nu\mu}[1-\frac{2n\nu\mu}{e^{\zeta}}-e^{-2\zeta}(1+a_0^2(\phi))]}, \tag{5}$$

where $a_0(\phi)$ puts emphasis on the longitudinal ponderomotive broadening by the variation of the intensity in the course of a pulse, $0<a_0(\phi)\le a_0$, and $\mu\neq 1$ accounts for the bandwidth effects, i.e., there is a distribution of laser frequencies around the central frequency ν. These effects are seen best in very backward kinematics, where $e^{2\zeta}(1-\cos(\pi-\Theta'))\to 0$: the support of harmonic n is in the interval $(1+\frac{e^{-\zeta}}{2n\nu\mu}(1+a_0^2))^{-1}\le 2e^{-\zeta}\nu'\le(1+\frac{e^{-\zeta}}{2n\nu\mu})^{-1}$ and depends additionally on the frequency spread parametrized by μ. The net effect is blowing up the curves $\nu'(n,\Theta')$ in the right panels of Figs. 4 and 5 to overlapping bands (not displayed), already either for $a_0\ge 1$ or $0.5<\mu<2$ separately. Both effects, $a_0(\phi)$ and $\mu\neq 1$, can be separated only in certain asymptotic regions [56]. Besides rich substructures within the broadened and overlapping harmonic support regions, QED calculations for laser pulses exhibit complicated interference patterns over the ω'-Θ' plane depending on the actual pulse envelope shape $g(\phi)$ and its parameters; see Fig. 1 in [58] for an example.

Nevertheless, the model (1) can provide a useful guide for the gross shape of the locally averaged spectrum. Averaging the differential cross section, exhibited in Fig. 7 (left) by the blue curve, over the intervals $\omega'(\ell-0.5,\Theta')\cdots\omega'(\ell+0.5,\Theta')$ for $\ell=1,2,3\cdots$[5] leads to the spectral shape displayed by blue bullets in the right panel of Fig. 7. Within a factor of 2, both spectral shapes—the one based on the monochromatic model (1) and the one with $1/\cosh$ pulse envelope—agree over 6 orders of magnitude. The displacement of pair-wise related red crosses and blue bullets in the right panel of Fig. 7 can be attributed to the frequency difference in (5) for $\nu'(a_0)$ and $\nu'(a_0=0)$ at the same value of n when ignoring the bandwidth effect.

If one wishes to recover the clear harmonic structures exhibited in Fig. 5, right, one has to employ suitable laser pulse shapes, e.g., with extended flat-top profiles (see Fig. 6 in [57]) or frequency chirping [59], etc. Nevertheless, we argue that these details, which shape the differential spectra, have a subleading impact on the phase space integrated cross section, and the prediction in Fig. 3 is essentially robust within the range uncovered by our pulsed QED calculations (red curves marked by bullets) and the model (1) (red solid curves).

[5]The continuous variable ℓ is an internal auxiliary quantity which replaces the harmonic number n in the case of a pulse with smoothly varying envelope (cf. qs. (16) and (17) in [56]).

In addition to such effects, there is transverse broadening with respect to multiple photon emission: the incoming electron may suffer a (or many) transverse kick(s) due to soft-photon emission prior to hard-photon emission, thus not being longer subject of a head-on collision. Since for the above LUXE kinematics our focus is on the hard-photon tail, e.g., with $\omega' > \frac{1}{2} p_0$ for $c = 1$, we do not expect a significant impact of the leakage of low harmonics into this region and multiple photon emission and radiation reaction as well. For a proper quantitative account, the simulation tools developed in view of the recent experiments [60,61] should be employed in dedicated analyses and compared with analog QED calculations.

VII. SUMMARY

In summary, we point out that the nonlinear Compton process obeys a field strength dependence $\propto \mathcal{P} \exp\{-a_{n\ell C} E_{\rm crit}/E\}$, similar to the Schwinger process of "vacuum break down,"when imposing a suitable cutoff c which suppresses the low harmonics. We focus on the slope coefficient $a_{n\ell C} = \frac{2}{3} cm/(p_0 + \sqrt{p_0^2 - m^2})$ by a comparison with some approximation formula which displays a dependence $\propto \exp\{-2c/3\chi\}$ already in the nonasymptotic region. Albeit the Compton process does not have such an obvious tunneling regime as the pair production processes, its formal similarity with the nonlinear Breit-Wheeler process provides evidence [48,62] for selected *differential* contributions with an exponential field dependence. The here introduced cutoff acts as a threshold and enforces a large gap between in- and out-Zel'dovich levels (which suffer some broadening in laser pulses) or, equivalently, a large light-cone momentum transfer from the in-electron to the out-photon; it makes the otherwise hidden exponential contributions visible in the total cross section, which actually refers to a fraction of the out-phase space. This opens another avenue toward a measurement of the boiling point of the vacuum, complementary to plans of the LUXE Collaboration by utilizing the nonlinear Breit-Wheeler pair production [32]. While for the latter one a high-energy photon beam is vital, our approach requires either a moderately high-energy (p_0) electron beam and the selection of very high harmonics or a high-energy electron beam and the selection of moderately high harmonics. The experimental challenge is anyway the isolation of the high harmonics region characterized by the out-photon kinematics.

The present considerations apply primarily to a plane-wave, monochromatic laser beam, i.e., a long flat-top pulse duration, with circular polarization. Selected examples of one-photon emission in laser pulses, based on Furry picture QED calculations of the cross section, support such a clear-cut approach. Nevertheless, necessary obvious extensions should take into account general laser polarizations as well as further bandwidth effects, ponderomotive broadening and multiple photon emissions in finite-duration pulses and their detailed temporal structures together with a larger range of the laser intensity parameter a_0. Planned follow-up work is devoted to energy and angular differential spectra and suitable realizations of the crucial cutoff implementation in nonperfect head-on collisions.

ACKNOWLEDGMENTS

The authors gratefully acknowledge the collaboration with D. Seipt, T. Nousch, and T. Heinzl, and useful discussions with A. Ilderton, K. Krajewska, M. Marklund, C. Müller, S. Rykovanov, R. Schützhold, and G. Torgrimsson. A. Ringwald is thanked for explanations with respect to LUXE. The work was supported by R. Sauerbrey and T. E. Cowan with respect to the study of fundamental QED processes for Helmholtz International Beamline for Extreme Fields at the European XFEL (HIBEF).

[1] F. Sauter, Über das Verhalten eines Elektrons im homogenen elektrischen Feld nach der relativistischen Theorie Diracs, Z. Phys. **69**, 742 (1931).
[2] W. Heisenberg and H. Euler, Consequences of Dirac's theory of positrons, Z. Phys. **98**, 714 (1936).
[3] J. S. Schwinger, On gauge invariance and vacuum polarization, Phys. Rev. **82**, 664 (1951).
[4] G. A. Mourou, T. Tajima, and S. V. Bulanov, Optics in the relativistic regime, Rev. Mod. Phys. **78**, 309 (2006).
[5] A. Di Piazza, C. Müller, K. Z. Hatsagortsyan, and C. H. Keitel, Extremely high-intensity laser interactions with fundamental quantum systems, Rev. Mod. Phys. **84**, 1177 (2012).
[6] G. Torgrimsson, C. Schneider, and R. Schützhold, Sauter-Schwinger pair creation dynamically assisted by a plane wave, Phys. Rev. D **97**, 096004 (2018).
[7] G. Torgrimsson, C. Schneider, J. Oertel, and R. Schützhold, Dynamically assisted Sauter-Schwinger effect—non-perturbative versus perturbative aspects, J. High Energy Phys. 06 (2017) 043.
[8] C. Fey and R. Schützhold, Momentum dependence in the dynamically assisted Sauter-Schwinger effect, Phys. Rev. D **85**, 025004 (2012).
[9] G. V. Dunne, H. Gies, and R. Schützhold, Catalysis of Schwinger vacuum pair production, Phys. Rev. D **80**, 111301 (2009).

[10] R. Schützhold, H. Gies, and G. Dunne, Dynamically Assisted Schwinger Mechanism, Phys. Rev. Lett. **101**, 130404 (2008).
[11] I. A. Aleksandrov, G. Plunien, and V. M. Shabaev, Dynamically assisted Schwinger effect beyond the spatially-uniform-field approximation, Phys. Rev. D **97**, 116001 (2018).
[12] I. A. Aleksandrov, G. Plunien, and V. M. Shabaev, Electron-positron pair production in external electric fields varying both in space and time, Phys. Rev. D **94**, 065024 (2016).
[13] M. Orthaber, F. Hebenstreit, and R. Alkofer, Momentum spectra for dynamically assisted schwinger pair production, Phys. Lett. B **698**, 80 (2011).
[14] A. Otto and B. Kämpfer, Afterglow of the dynamical Schwinger process: Soft photons amass, Phys. Rev. D **95**, 125007 (2017).
[15] A. D. Panferov, S. A. Smolyansky, A. Otto, B. Kämpfer, D. B. Blaschke, and L. Juchnowski, Assisted dynamical Schwinger effect: Pair production in a pulsed bifrequent field, Eur. Phys. J. D **70**, 56 (2016).
[16] A. Otto, D. Seipt, D. Blaschke, S. A. Smolyansky, and B. Kämpfer, Dynamical Schwinger process in a bifrequent electric field of finite duration: Survey on amplification, Phys. Rev. D **91**, 105018 (2015).
[17] A. Otto, D. Seipt, D. Blaschke, B. Kämpfer, and S. A. Smolyansky, Lifting shell structures in the dynamically assisted Schwinger effect in periodic fields, Phys. Lett. B **740**, 335 (2015).
[18] A. Otto, T. Nousch, D. Seipt, B. Kämpfer, D. Blaschke, A. D. Panferov, S. A. Smolyansky, and A. I. Titov, Pair production by Schwinger and Breit-Wheeler processes in bifrequent fields, J. Plasma Phys. **82**, 655820301 (2016).
[19] G. Torgrimsson, J. Oertel, and R. Schutzhold, Doubly assisted Sauter-Schwinger effect, Phys. Rev. D **94**, 065035 (2016).
[20] A. Otto, H. Oppitz, and B. Kämpfer, Assisted vacuum decay by time dependent electric fields, Eur. Phys. J. A **54**, 23 (2018).
[21] S. S. Bulanov, V. D. Mur, N. B. Narozhny, J. Nees, and V. S. Popov, Multiple Colliding Electromagnetic Pulses: A Way to Lower the Threshold of e^+e^- Pair Production from Vacuum, Phys. Rev. Lett. **104**, 220404 (2010).
[22] F. Hebenstreit and F. Fillion-Gourdeau, Optimization of Schwinger pair production in colliding laser pulses, Phys. Lett. B **739**, 189 (2014).
[23] C. Kohlfürst, M. Mitter, G. von Winckel, F. Hebenstreit, and R. Alkofer, Optimizing the pulse shape for Schwinger pair production, Phys. Rev. D **88**, 045028 (2013).
[24] N. D. Birell and P. C. Davies, *Quantum Fields in Curved Space* (Cambridge University Press, Cambridge, United Kingdom, 1982).
[25] S. W. Hawking, Particle creation by black holes, Commun. Math. Phys. **43**, 199 (1975); Erratum, Commun. Math. Phys. **46**, 206 (1976).
[26] W. G. Unruh, Notes on black hole evaporation, Phys. Rev. D **14**, 870 (1976).
[27] L. C. B. Crispino, A. Higuchi, and G. E. A. Matsas, The Unruh effect and its applications, Rev. Mod. Phys. **80**, 787 (2008).
[28] N. B. Narozhny, A. M. Fedotov, B. M. Karnakov, V. D. Mur, and V. A. Belinskii, Reply to comment on 'Boundary conditions in the Unruh problem', Phys. Rev. D **70**, 048702 (2004).
[29] M. F. Linder, A. Lorke, and R. Schützhold, Analog Sauter-Schwinger effect in semiconductors for spacetime-dependent fields, Phys. Rev. B **97**, 035203 (2018).
[30] F. Dreisow, S. Longhi, S. Nolte, A. Tunnermann, and A. Szameit, Vacuum Instability and Pair Production in an Optical Setting, Phys. Rev. Lett. **109**, 110401 (2012).
[31] S. Lang and R. Schützhold, Analog of cosmological particle creation in electromagnetic waveguides, Phys. Rev. D **100**, 065003 (2019).
[32] A. Hartin, A. Ringwald, and N. Tapia, Measuring the boiling point of the vacuum of quantum electrodynamics, Phys. Rev. D **99**, 036008 (2019).
[33] M. Altarelli *et al.*, Summary of strong-field QED Workshop, arXiv:1905.00059.
[34] H. Abramowicz *et al.*, Letter of intent for the LUXE experiment, arXiv:1909.00860.
[35] D. L. Burke *et al.*, Positron Production in Multi-photon Light by Light Scattering, Phys. Rev. Lett. **79**, 1626 (1997).
[36] V. Dinu and G. Torgrimsson, Trident pair production in plane waves: Coherence, exchange, and spacetime inhomogeneity, Phys. Rev. D **97**, 036021 (2018).
[37] V. Dinu and G. Torgrimsson, Trident process in laser pulses, Phys. Rev. D **101**, 056017 (2020).
[38] V. N. Baier, V. M. Katkov, and V. M. Strakhovenko, Higher-order effects in external field—pair production by a particle, Yad. Fiz. **14**, 1020 (1971) [Sov. J. Nucl. Phys. **14**, 572 (1972)].
[39] V. I. Ritus, Vacuum polarization correction to elastic electron and muon scattering in an intense field and pair electro- and muoproduction, Nucl. Phys. **B44**, 236 (1972).
[40] C. Harvey, T. Heinzl, and A. Ilderton, Signatures of high-intensity compton scattering, Phys. Rev. A **79**, 063407 (2009).
[41] L. D. Landau and E. M. Lifshitz, *Quantum Electrodynamics*, 2nd ed. (Pergamon, New York, 1982).
[42] A. Jochmann *et al.*, High Resolution Energy-Angle Correlation Measurement of Hard X Rays from Laser-Thomson Backscattering, Phys. Rev. Lett. **111**, 114803 (2013).
[43] I. C. E. Turcu *et al.*, High field physics and QED experiments at ELI-NP, Rom. Rep. Phy. **68**, S145 (2016), https://www.researchgate.net/publication/303365338_High_field_physics_and_QED_experiments_at_ELI-NP.
[44] T. Nousch, D. Seipt, B. Kämpfer, and A. I. Titov, Pair production in short laser pulses near threshold, Phys. Lett. B **715**, 246 (2012).
[45] A. I. Titov, A. Otto, and B. Kämpfer, Multi-photon regime of non-linear Breit-Wheeler and Compton processes in short linearly and circularly polarized laser pulses, Eur. Phys. J. D **74**, 39 (2020).
[46] A. I. Titov, H. Takabe, B. Kämpfer, and A. Hosaka, Enhanced Subthreshold Electron-Positron Production in Short Laser Pulses, Phys. Rev. Lett. **108**, 240406 (2012).
[47] H. R. Reiss, Absorbtion of light by light, J. Math. Phys. (N.Y.) **3**, 59 (1962).
[48] V. I. Ritus, Quantum effects of the interaction of elementary particles with an intense electromagnetic field, J. Sov. Laser Res. (United States) **6**, 497 (1985).

[49] A. I. Nikishov and V. I. Ritus, Quantum processes in the field of a plane electromagnetic wave and in a constant field I; II, Sov. Phys. JETP **19**, 529 (1964); **19**, 1191 (1964); **25**, 1135 (1967).
[50] T. Podszus and A. Di Piazza, High-energy behavior of strong-field QED in an intense plane wave, Phys. Rev. D **99**, 076004 (2019).
[51] A. Ilderton, Note on the conjectured breakdown of QED perturbation theory in strong fields, Phys. Rev. D **99**, 085002 (2019).
[52] I. Aniceto, G. Basar, and R. Schiappa, A primer on resurgent transseries and their asymptotics, Phys. Rep. **809**, 1 (2019).
[53] N. B. Narozhnyi and M. S. Fofanov, Photon emission by an electron in a collision with a short focused laser pulse, Zh. Eksp. Teor. Fiz. **110**, 26 (1996) [J. Exp. Theor. Phys. **83**, 14 (1996)].
[54] T. Heinzl, B. King, and A. J. Macleod, The locally monochromatic approximation to QED in intense laser fields, arXiv:2004.13035.
[55] D. Seipt, Strong-field QED processes in short laser pulses, Ph.D. thesis, TU Dresden, 2012.
[56] A. I. Titov, B. Kämpfer, T. Shibata, A. Hosaka, and H. Takabe, Laser pulse-shape dependence of Compton scattering, Eur. Phys. J. D **68**, 299 (2014).
[57] D. Seipt and B. Kämpfer, Non-linear compton scattering of ultrashort and ultraintense laser pulses, Phys. Rev. A **83**, 022101 (2011).
[58] D. Seipt and B. Kämpfer, Non-linear Compton scattering of ultrahigh-intensity laser pulses, Laser Phys. **23**, 075301 (2013).
[59] D. Seipt, S. G. Rykovanov, A. Surzhykov, and S. Fritzsche, Narrowband inverse Compton scattering x-ray sources at high laser intensities, Phys. Rev. A **91**, 033402 (2015).
[60] K. Poder *et al.*, Experimental Signatures of the Quantum Nature of Radiation Reaction in the Field of an Ultraintense Laser, Phys. Rev. X **8**, 031004 (2018).
[61] J. M. Cole *et al.*, Experimental Evidence of Radiation Reaction in the Collision of a High-Intensity Laser Pulse with a Laser-Wakefield Accelerated Electron Beam, Phys. Rev. X **8**, 011020 (2018).
[62] V. Dinu and G. Torgrimsson, Single and double nonlinear Compton scattering, Phys. Rev. D **99**, 096018 (2019).